

2016-03-28

Anomalous electron heating effects on the E region ionosphere in TIEGCM

Jing Liu, Wenbin Wang, Meers Oppenheim, Yakov Dimant, Michael Wiltberger, Slava Merkin.

2016. "Anomalous electron heating effects on the E region ionosphere in TIEGCM."

Geophysical Research Letters, Volume 43, Issue 6, pp. 2351 - 2358.

<https://hdl.handle.net/2144/27913>

"Downloaded from OpenBU. Boston University's institutional repository."

Anomalous Electron Heating Effects on the E-region Ionosphere in TIEGCM

Jing Liu¹, Wenbin Wang¹, Meers Oppenheim², Yakov Dimant², Michael Wiltberger¹, and Slava Merkin³

¹High Altitude Observatory, National Center for Atmospheric Research, Boulder, Colorado, USA

²Center for Space Physics, Boston University, Boston, Massachusetts, USA

³Space Department, Applied Physics Laboratory, Johns Hopkins University, Laurel, Maryland, USA

Corresponding author: Jing Liu (jingliu@ucar.edu)

Short Title: Anomalous Electron Heating in TIEGCM

46 **Abstract**

47 We have recently implemented a new module that includes both the anomalous electron
48 heating and the electron-neutral cooling rate correction associated with the Farley-Buneman
49 Instability (FBI) in the Thermosphere Ionosphere Electrodynamics Global Circulation Model
50 (TIEGCM). This implementation provides, for the first time, a modeling capability to describe
51 macroscopic effects of the FBI on the ionosphere and thermosphere in the context of a first
52 principle, self-consistent model. The added heating sources primarily operate between 100 and
53 130 km altitude and their magnitudes often exceed auroral precipitation heating in the TIEGCM.
54 The induced changes in E-region electron temperature in the auroral oval and polar cap by the
55 FBI are remarkable with a maximum T_e approaching 2200 K. This is about four times larger than
56 the TIEGCM run without FBI heating. This investigation demonstrates how researchers can add
57 the important effects of the FBI to magnetosphere-ionosphere-thermosphere models and
58 simulators.

59

60 **1. Introduction**

61 In the ionospheric E-region, electrons are magnetized (i.e. their gyro frequencies far exceed
62 their electron-neutral collision frequencies). Thus the electrons predominantly drift perpendicular
63 to the electric fields. In contrast, the ions are unmagnetized because their gyro frequencies are
64 smaller than their ion-neutral collision frequencies and neutral winds drag the ions. This
65 differential motion between the electrons and the ions becomes very large during geomagnetic
66 disturbed conditions, and will excite the Farley-Buneman Instability (FBI) [Farley, 1963;
67 Buneman, 1963]. Typically, the FBI becomes significant when difference between the drift
68 speeds of the electrons and ions exceeds the ion acoustic speed (~ 400 m/s). This instability leads

69 to turbulent electric fields and plasma density perturbations. The interaction of the electrons with
70 the turbulent electric fields caused by the FBI produces anomalous electron heating (AEH) in the
71 auroral and subauroral regions where electric fields are mapped from the magnetosphere and
72 thus ion-electron differential motion are large [e.g., Schlegel and St.-Maurice et al., 1981;
73 Providakes et al., 1988; Bahcivan, 2007; Oppenheim et al., 2013]. Note that AEH cannot be fully
74 explained by the frictional heating and auroral precipitation heating [Nielsen and Schlegel, 1985].

75 Numerous radar observations have shown dramatic enhancements of the electron temperature
76 in the subauroral and auroral electrojet regions during major geomagnetic storms as a result of
77 AEH [e.g., St.-Maurice and Laher, 1985; Foster and Erickson, 2000; Milikh et al., 2006;
78 Bahcivan, 2007]. AEH typically takes place at an altitude of between 105 and 125 km, and raises
79 the electron temperature from approximately 400 K to 4000 K. Robinson and Honary [1993]
80 developed a fluid model to reproduce the relationship between the electron drift velocity and
81 electron temperature in association with AEH. More recently, Dimant and Milikh [2003]
82 developed a more accurate kinetic model of electron heating by the FBI, taking into account the
83 effects of FBI induced turbulent electric fields parallel to the geomagnetic field [Milikh and
84 Dimant, 2002, 2003]. We will use the results of this model in the Thermosphere Ionosphere
85 Electrodynamics General Circulation Model (TIEGCM).

86 Merkin et al. [2005] included a simplified version of the effect of the FBI on ionospheric
87 conductance in a global MHD magnetospheric model. They showed that ionospheric
88 conductance changes associated with the FBI results in significant changes in cross-polar cap
89 potential and the strength of the high-latitude convection electric field. Since electric fields play
90 an essential role in determining the amount of energy and momentum deposition from the
91 magnetosphere into the upper atmosphere, the small-scale ionospheric FBI can have a large

92 impact on the global coupled ionosphere-magnetosphere system.

93 The current paper describes a method of incorporating AEH into the state-of-the-art
94 TIEGCM and shows the importance of doing so. It shows that turbulence has a comparable and
95 often larger effect on electron temperatures than precipitation does. This means that including
96 AEH in ionosphere and coupled magnetosphere-ionosphere models is essential to accurately
97 modeling storm-time events.

98

99 2. Model description

100 The TIEGCM is a comprehensive, three-dimensional, time-dependent, non-linear
101 representation of the coupled ionosphere and thermosphere system that solves momentum,
102 energy and continuity equations for neutral and ion species [Roble et al., 1988; Richmond et al.,
103 1992]. The TIEGCM in this study has a horizontal resolution of 2.5° and vertical resolution of a
104 quarter of a scale height. Ionospheric convection electric fields at high latitudes are specified
105 using the Weimer model [2005]. We use the default auroral precipitation model that is based on
106 the estimated hemispheric power of precipitating electrons [Roble and Ridley, 1987]. For this
107 study, we assume conditions typical of an intense geomagnetic storm driven by an interplanetary
108 coronal mass ejection. Specifically, constant IMF Bz (-20 nT), IMF By (0 nT), and solar wind
109 velocity (1000 km/s) during September equinox are used for medium solar activity conditions
110 (F10.7 = 120) [Gopalswamy, 2006].

111 TIEGCM conserves electron energy by solving for the electron temperature by applying,

$$112 \sin^2 I \frac{\nabla}{H \nabla z} (K^e \frac{\nabla T_e}{H \nabla z}) + \dot{a} Q_e - \dot{a} L_e = 0 \quad (1)$$

113 where I is geomagnetic dip angle, H is the neutral scale height, K^e is the electron thermal
114 conductivity coefficient, Q_e is the heating rate and L_e is the thermal loss rate [Schunk and Nagy,

115 1978]. To include the effects of turbulent electron heating in the E-region, we modified both Q_e
 116 and L_e .

117 To do this, we add the following terms (Q_a) to Q_e :

$$118 \quad Q_a = \frac{m_e \nu_e n_0 E^2}{B^2} + \frac{m_i \nu_i n_0 \kappa_i^2 (E - E_1)^2}{(1 + \kappa_i^2) B^2} \left(\frac{E}{E_1} (1 + \psi) - 1 \right) H(E - E_1) H(h_{MB} - h), \quad (2)$$

119 where

$$120 \quad E_1 = (1 + \psi) \sqrt{\frac{K_b (1 + \kappa_i^2)}{1 - \kappa_i^2} \left(\frac{T_e + T_i}{m_i} \right)} B, \quad (3)$$

$$121 \quad \psi = \frac{\nu_e \nu_i}{\Omega_e \Omega_i} = \frac{m_e \nu_e m_i \nu_i}{e^2 B^2}, \quad \text{and} \quad (4)$$

$$122 \quad \kappa_i = \frac{\Omega_i}{\nu_i} = \frac{eB}{m_i \nu_i} \quad (5)$$

123 Here, B is the strength of the geomagnetic field; K_b is the Boltzmann constant; $m_{e,i}$ are the
 124 masses of the electrons and ions, respectively; e is the elementary charge; T_e and T_i are electron
 125 and ion temperatures; Ω_i is the ion gyro-frequency; and ν_i is the ion-neutral collision
 126 frequency.

127 The first term on the right-hand side of Eq. (2) is the electron Ohmic energy deposition ($\mathbf{J} \cdot \mathbf{E}$)
 128 that occurs as electrons are forced to travel through the neutral medium by the large-scale
 129 electric fields (E). The second term approximates the effect of turbulent heating by Farley-
 130 Buneman turbulence as discussed in Dimant and Milikh (2003) and Dimant and Oppenheim
 131 (2011). $H(x)$ is a step function that prevents AEH from becoming active when the instability
 132 driving electric fields E falls below the threshold electric field E_1 . $H(x)$ is also used to eliminate
 133 heating above the ion magnetization boundary h_{MB} where the ion gyro frequency Ω_i equals the
 134 ion-neutral collision frequency ν_i , a region where little to no turbulence should develop. This

135 term has been validated by using large-scale 3D kinetic simulations of Farley-Buneman
136 turbulence [Oppenheim and Dimant, 2013].

137 In addition to the strong electron heating associated with the FBI, we have also introduced a
138 temperature-dependent multiplier for the electron-neutral cooling rate L_e . We need this for the
139 following reason. The previous electron cooling rate assumes a Maxwellian distribution function
140 of electrons. This is appropriate for moderate temperature increases, but is unacceptable for the
141 intense temperature elevations caused by the AEH effect. According to the kinetic simulations by
142 Milikh and Dimant [2003, Fig. 1], as the electron temperature increases by more than a factor of
143 three, a significant reduction of super-thermal electron velocities develops. This non-Maxwellian
144 distribution has a significantly reduced electron cooling rate as seen in Milikh and Dimant (2003),
145 Fig. 4. We add this effect to TIEGCM by reducing the electron thermal loss rate, L_e , by a factor
146 (L_a) of

$$147 L_a(T_e) = e^{-7.54 \times 10^{-4}(T_e - 500)} \quad (6)$$

148 This only applies for $T_e > 500$ K, otherwise we set $L_a = 1$. This approximation should model this
149 kinetic effect with sufficient accuracy for the purposes of accurately capturing AEH.

150

151 3. Results and Analysis

152 In order to understand the effects of the AEH on the storm-time upper atmosphere, we
153 compared a series of simulations that included the AEH effects with those not including them.
154 For simplicity, hereafter TIEGCM and TIEGCM- κ denote default TIEGCM run and TIEGCM
155 run that included AEH effect, respectively. Note that all simulations were driven with exactly the
156 same geophysical conditions (Section 2). Figure 1 compares (a) regular electron Ohmic energy
157 deposition, (b) anomalous electron energy deposition, (c) TIEGCM auroral precipitation energy

158 deposition (in units of $\text{J}\cdot\text{m}^{-3}\cdot\text{s}^{-1}$), for (d) the externally imposed convection electric field (E_c , in
159 units of mV/m) at pressure level -4.375 (~ 112 km) in the geographic coordinates. Both regular
160 electron Ohmic energy deposition and anomalous electron energy deposition generally peak in
161 the postmidnight to early morning sectors (0200-0700 LT) in the auroral oval. The magnitudes of
162 the anomalous electron energy deposition are comparable to or even larger than the magnitude of
163 the TIEGCM auroral precipitation heating source. The TIEGCM auroral precipitation energy
164 deposition is more extended in latitude and closer to postmidnight. The regular electron Ohmic
165 energy deposition is generally smaller than the anomalous electron energy deposition on this
166 pressure level.

167 The maximum E_c is ~ 86 mV/m , which far exceeds the F-B turbulence electric field threshold
168 of ~ 40 mV/m (see, Eq. (2)). E_c has large values in the following regions: in the geographic
169 latitude range of 70 - 80° around 0000 LT, around geographic latitude 70° within 0300-0600 LT,
170 and near geographic latitudes 75 - 85° in the afternoon sector. Regular electron Ohmic energy
171 deposition and anomalous electron energy deposition do not follow the distribution of E_c ,
172 because they are also modulated by electron density and collision frequency. Thus, the calculated
173 anomalous electron energy deposition is weighted by the polar E-region electron density that is
174 caused by auroral precipitation and typically peaks in the auroral oval.

175 We can directly compare runs with and without AEH. Figure 2 compares a polar view of the
176 electron temperatures (Figures 2a, 2b and 2c) and electron densities (Figures 2e, 2f and 2g) with
177 and without the AEH heating sources, as well as their differences in the geographic coordinates.
178 The absolute differences of Hall conductivity and Pedersen Conductivity (in units of S/m) for
179 these two cases are displayed in Figures 2d and 2h, respectively. Electron temperature
180 enhancements at high latitudes are generally of ~ 500 to ~ 2000 K. A region of high temperatures

181 with the maximum approaching 2200 K can be seen within the latitude range of 70-80° at around
182 0000 LT. This T_e increase is about a factor of 5 larger than the background T_e .

183 Radars have observed large electron temperature enhancement in the E region ranging from
184 300 K to 4000 K in the presence of large electric fields during major geomagnetic storm
185 [Schlegel and St.-Maurice, 1981; Providakes et al., 1988; Foster and Erickson, 2000; Bahcivan,
186 2007]. The TIEGCM-k predicted that T_e enhancements also occur in the location of radar
187 observed large T_e enhancements.

188 The distribution of T_e enhancements follows almost exactly the distribution of E_c . If we only
189 consider the AEH effect, the electron energy equation can be formulated:

$$190 \quad Q_a - Cooling = 0 \quad (7)$$

191 where *Cooling* is proportional to $n_0(T_e - T_n)$. n_0 is electron densities and T_n is neutral temperature.

192 Comparing Eqs. (2) and (7), we can see that electron temperature changes are related to E_c but
193 not electron densities since both sides of this equation are proportional to n_0 . This can explain the
194 approximate linear increase of electron temperatures with E_c [Schlegel and St.-Maurice, 1981;
195 Williams et al., 1992; Foster and Erickson, 2000].

196 A T_e enhancement in the E region reduces molecular recombination rate and increases electron
197 densities [Schlegel, 1982]. As shown in the right panel of Figure 2 (Figure 2g), the peak electron
198 density in the auroral oval increased by about $3 \times 10^5 \text{ cm}^{-3}$, corresponding to an about 60%
199 increase in the postmidnight sector.

200 Both electron temperature and density changes affect ionospheric conductivities. Notice that
201 this paper does not include the additional anomalous effect of the nonlinear current, which
202 should result in an additional increase in the Pedersen conductivity [Oppenheim et al., 1997;
203 Dimant and Oppenheim, 2011]. The Hall and Pedersen conductivity changes distribute in similar

204 patterns and are restricted in the altitude range between 100 and 120 km. Hall and Pedersen
205 conductivities have $3\sim 10\times 10^{-4}$ S/m and $7\times 10^{-5}\sim 3\times 10^{-4}$ S/m enhancement, corresponding to 40%-
206 80% and 26%-88% increase in the auroral oval, respectively. General agreements exist between
207 our results and simulation outcome from Dimant and Oppenheim [2011] (Figure 5) that showed
208 the largest Pedersen conductivity enhancement occurring at around 116 km and were close to 60 %
209 in the absence of nonlinear current induced anomalous conductivity.

210 As displayed in Figure 1, the two energy dissipation sources have larger values at around
211 0400 Local Time (LT) in the Northern Hemisphere. Figure 3 shows a latitudinal and altitudinal
212 slice of the difference in T_e and N_e with and without AEH at 0400 LT. It is evident that the T_e
213 enhancements mainly take place at high latitudes within the altitude ranges between 101 and 116
214 km and center at around 110 km. The relative enhancements of T_e are about 200%. Similarly, N_e
215 increases are about 50%-70% and also generally occur at around 110 km. There is also evident
216 north-south asymmetry in T_e and N_e enhancements.

217 Figure 4 depicts the electron temperature profiles at two locations with the largest increased
218 T_e as shown in Figure 2. The blue and red lines are the results of the default TIEGCM run
219 without AEH and the run including AEH, respectively. The top panel, which is within a
220 geographic latitude range $70\text{-}80^\circ$ around 0000 LT, shows that the maximum T_e is about 2200 K
221 and occurs at around 114 km when E_c equals to 86 mV/m. The bottom panel corresponds to a
222 high T_e region at around geographic latitude 60° and between 0300 and 0600 LT. The T_e profile
223 with AEH has a maximum value of about 1300 K at around 110 km where E_c has the value of \sim
224 40 mV/m. It is of interest to compare the results with Figure 3 of Bahcivan [2007] in which the
225 electron temperatures were close to 2000 K and 1000 K when E_c had values of about 80 mV/m
226 and 40 mV/m, respectively. This also agrees well with the model result of Dimant and

227 Oppenheim [2011] that the maximum electron temperature of ~2000 K occurred at 112 km when
228 $E_c=80$ mV/m.

229

230 **4. Summary and Future Work**

231 For the first time, AEH and kinetically decreased electron collisional cooling rates associated
232 with the FBI have been implemented in a physics-based, coupled ionosphere-thermosphere
233 model (TIEGCM). The TIEGCM was driven by high-latitude convection electric fields from the
234 Weimer model under strong solar wind driven condition and medium solar activity in September
235 equinox. AEH source terms are most prominent in the early morning sector and are comparable
236 in magnitude to, or even larger than the magnitude of auroral precipitation heating in the E
237 region. Intense electron heating reduces plasma recombination rate leading to a dramatic local
238 increase in the E-region plasma density [St.-Maurice, 1990; Milikh and Dimant, 2003; Milikh et
239 al., 2006]. As plasma density increases, both the Hall and Pedersen conductivities increase in
240 proportion. The maximum changes in electron temperature, density, Pedersen conductivity are
241 ~2200 K, 3×10^5 cm⁻³, 3×10^{-4} S/m, corresponding to ~400%, 60%, and 88% increases relative to
242 their background values, respectively.

243 The conductance changes have important effects on the coupling between the magnetosphere
244 and ionosphere. These will feedback to the cross-polar cap potential and the evolution of field-
245 aligned currents. Merkin et al. [2005] revealed that the global magnetosphere model (LFM) more
246 successfully reproduces with the convection pattern than does the Assimilative Mapping of
247 Ionospheric Electrodynamics (AMIE), which is a data driven model. LFM also better
248 reproduces Defense Meteorological Satellite Program (DMSP) satellite measurements after
249 including parameterized AEH effects.

250 The Weimer model tends to underestimate the convection electric fields due to statistical
251 smoothing of potentials [Weimer, 2005]. A larger electric field would lead to even more
252 significant heating by AEH. In future work, we are planning to replace the Weimer model for
253 driving TIEGCM at high-latitudes by the LFM, which has been coupled to TIEGCM in a
254 complete magnetosphere-ionosphere-thermosphere (CMIT) simulator [Wang et al., 2004;
255 Wiltberger et al., 2004]. This will allow us to study the effects of higher driving electric fields
256 and the feedback of FBI-driven conductance increases on the global magnetospheric processes.

257 The FBI affects the ionosphere in two distinct ways: (1) it causes AEH that raises the electron
258 temperature; (2) it also drives nonlinear currents, increasing the ion-dominated Pedersen
259 conductivity. In the current work, we only deal with the AEH effect on the ionosphere. Dimant
260 and Oppenheim [2011] pointed out that the Pedersen Conductance change can reach 150%
261 relative to the background value for $E_c=80$ mv/m after taking both AEH and nonlinear currents
262 effects into consideration. In future work, we will also incorporate the FBI induced ionospheric
263 Pedersen conductivity in the TIEGCM-κ, and to add these Farley-Buneman nonlinear currents
264 effects into the coupled magnetosphere ionosphere thermosphere model to fully evaluate the
265 effects of these small-scale processes on the changes of geospace environment during major
266 geomagnetic storms.

267 This investigation presents a significant advance in understanding cross-scale coupling within
268 the geospace system. It has important implications for space weather research as it adds new
269 physics to a first-principle global thermosphere and ionosphere model. It demonstrates that the
270 FBI effects on the storm-time ionosphere can exceed the effects of precipitation and Joule
271 heating of the electrons. This research substantially improves researcher's abilities to simulate
272 the dynamic and nonlinear response of the magnetosphere-ionosphere-thermosphere system to

273 geomagnetic storms over a large range of spatial and temporal scales.

274

275 **Acknowledgement**

276 The authors thank Dr. Art Richmond for his insightful comments. This work is supported by
277 NASA GCR grants NNX14A113G. This work is also supported in part by NASA LWS grants
278 NNX14AE06G, and NNX15AB83G, and NASA HGI grant NNX12AJ54G. The National Center
279 for Atmospheric Research is sponsored by the National Science Foundation. This work used the
280 Extreme Science and Engineering Discovery Environment (XSEDE), which is supported by
281 National Science Foundation grant number ACI-1053575. The simulation data are accessible
282 upon request (jingliu@ucar.edu).

283

284 **References**

- 285 Bahcivan, H. (2007), Plasma wave heating during extreme electric fields in the high-latitude E
286 region, *Geophys. Res. Lett.*, 34, L15106, doi: 10.1029/2006GL029236.
- 287 Buneman, O., Excitation of field aligned sound waves by electron streams, *Phys. Rev. Lett.*, 10,
288 285-287, 1963.
- 289 Dimant, Y. S., and G. M. Milikh (2003), Model of anomalous electron heating in the E region: 1.
290 Basic theory, *J. Geophys. Res.*, 108(A9), 1350, doi: 10.1029/2002JA009524.
- 291 Dimant, Y. S. and M. M. Oppenheim (2011), Magnetosphere-ionosphere coupling through E
292 region turbulence: 2. Anomalous conductivities and frictional heating. *J. Geophys. Res.*,
293 116:A09304, doi: 10.1029/2011JA016649.
- 294 Farley, D. T., A plasma instability resulting in field-aligned irregularities in the ionosphere, *J.*
295 *Geophys. Res.*, 68, 6083-6097, 1963.
- 296 Foster, J. C., and P. J. Erickson, Simultaneous observations of E-region coherent backscatter and
297 electric field amplitude at F-region heights with the Millstone Hill ULF radar, *Geophys. Res.*
298 *Lett.*, 27, 3177-3180, 2000.
- 299 Gopalswamy, N. (2006), Coronal mass ejections of solar cycle 23, *J. Astrophys. Astron.*, 27,
300 243-254.
- 301 Lyon, J. G., J. A. Fedder, and C. M. Mobarry (2004), The Lyon-Fedder-Mobarry (LFM) global
302 MHD magnetospheric simulation code, *J. Atmos. Sol. Terr. Phys.*, 66, 1333-1350, doi:
303 10.1016/j.jastp.2004.03.020.
- 304 Merkin, V. G., G. Milikh, K. Papadopoulos, J. Lyon, Y. S. Dimant, A. S. Sharma, C. Goodrich,
305 and M. Wiltberger (2005), Effect of anomalous electron heating on the transpolar potential
306 in the LFM global MHD model, *Geophys. Res. Lett.*, 32, L22101,
307 doi:10.1029/2005GL023315.
- 308 Milikh, G. M., and Y. S. Dimant (2002), Kinetic model of electron heating by turbulent electric
309 field in the E region, *Geophys. Res. Lett.*, 29(12), doi:10.1029/2001GL013935.
- 310 Milikh, G. M., and Y. S. Dimant (2003), Model of anomalous electron heating in the E region: 2.
311 Detailed numerical modeling, *J. Geophys. Res.*, 108(A9), 1351, doi:10.1029/2002JA009527.
- 312 Milikh, G. M., L. P. Goncharenko, Y. S. Dimant, J. P. Thayer, and M. A. McCready (2006),
313 Anomalous electron heating and its effect on the electron density in the auroral electrojet,
314 *Geophys. Res. Lett.*, 33, L13809, doi:10.1029/2006GL026530.

315 Nielsen, E., and K. Schlegel (1985), Coherent radar Doppler measurements and their relationship
316 to the ionospheric electron drift velocity, *J. Geophys. Res.*, 90, 3498.

317 Oppenheim, M. M., and Y. S. Dimant (2013), Kinetic simulations of 3-D Farley-Buneman
318 turbulence and anomalous electron heating, *J. Geophys. Res. Space Physics*, 118, 1306–
319 1318, doi:10.1002/jgra.50196.

320 Oppenheim, M. M., A wave-driven nonlinear current in the E-region ionosphere, *Geophys. Res.*
321 *Let.*, Vol. 23, No. 23, 3333, 1996.

322 Providakes, J., D. T. Farley, B. G. Fejer, J. Sahr, and W. E. Swartz (1988), Observations of
323 auroral E-region plasma waves and electron heating with EISCAT and a VHF radar
324 interferometer, *J. Atmos. Terr. Phys.*, 50, 339-347.

325 Robinson, T. R. and Honary, F. (1993), Adiabatic and isothermal ion acoustic speeds of
326 stabilized Farley–Buneman waves in the auroral E-region, *J. Atmos. Terr. Phys.*, 55, 65-77.

327 Roble, R. G., and E. C. Ridley (1987), An auroral model for the NCAR thermospheric general
328 circulation model (TGCM), *Ann. Geophys.*, 5A(6), 369.

329 Roble, R. G., E. C. Ridley, A. D. Richmond, and R. E. Dickinson (1988), A coupled
330 thermosphere/ionosphere general circulation model, *Geophys. Res. Lett.*, 15, 1325-1328,
331 doi: 10.1029/GL015i012p01325.

332 Richmond, A. D., E. C. Ridley and R. G. Roble (1992), A Thermosphere/Ionosphere General
333 Circulation Model with coupled electrodynamics, *Geophys. Res. Lett.*, 19, 601-604.

334 Schlegel, K. (1982), Reduced effective recombination coefficient in the disturbed polar E-region,
335 *J. Atmos. Terr. Phys.*, 44, 183–185.

336 Schlegel, K., and J. P. St.-Maurice (1981), Anomalous heating of the polar E region by unstable
337 plasma waves: 1. Observations, *J. Geophys. Res.*, 86, 1447-1452.

338 Schunk, R. W., and A. F. Nagy (1978), Electron temperatures in the F region of the ionosphere:
339 Theory and observations, *Rev. Geophys.*, 15, 355–399.

340 St-Maurice, J. P., and R. Laher (1985), Are observed broadband plasma wave amplitude large
341 enough to explain the enhanced temperatures in the high-latitude E-region?, *J. Geophys.*
342 *Res.*, 90, 2843-2850, 1985.

343 St.-Maurice, J. P., Electron heating by plasma waves in the highlatitude E-region and related
344 effects: Theory, *Adv. Space Res.*, 10(6), 239–249, 1990.

345 Weimer, D. R. (2005), Predicting surface geomagnetic variations using ionospheric
346 electrodynamic models, *J. Geophys. Res.*, 110, A12307, doi: 10.1029/2005JA011270.

347 Wang, W., M. Wiltberger, A.G. Burns, S.C. Solomon, T.L. Killeen, N. Maruyama, and J.G.
348 Lyon (2004), Initial Results from the Coupled Magnetosphere-Ionosphere-Thermosphere
349 Model: Thermosphere-Ionosphere Responses, *J. Atmos. Solar-Terr. Phys.*, 66/15-16, 1425.

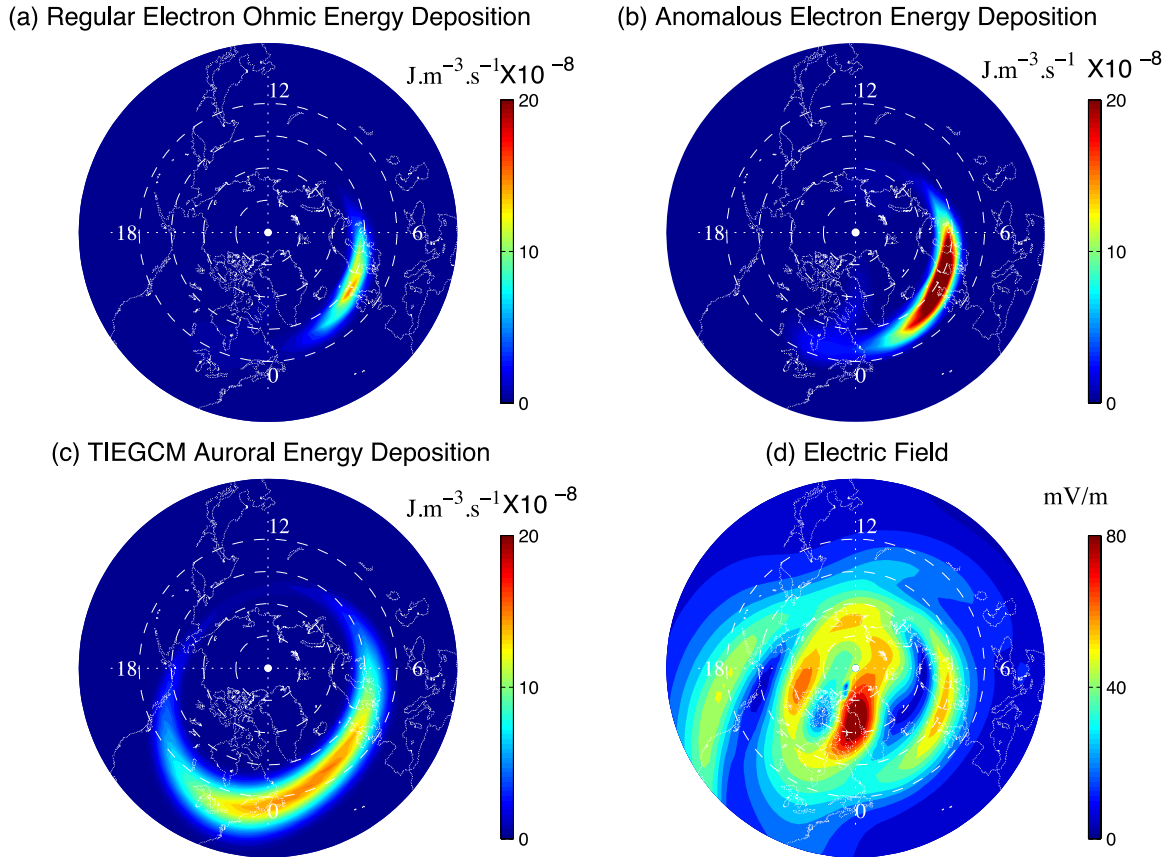
350 Wiltberger, M., Wang, W., Burns, A.G., Solomon, S.C., Lyon, J.G., Goodrich, C. C. (2004),
351 Initial results from the coupled magnetosphere ionosphere thermosphere model:
352 Magnetospheric and ionospheric responses, *J. Atmos. Solar-Terr. Phys.*, 66/15-16, 1411-
353 1424.

354 Williams, P. J. S., B. Jones, and G. O. L. Jones (1992), The measured relationship between
355 electric field strength and electron temperature in the auroral *E* region, *J. Atmos. Terr. Phys.*,
356 54, 741.

357
358
359
360

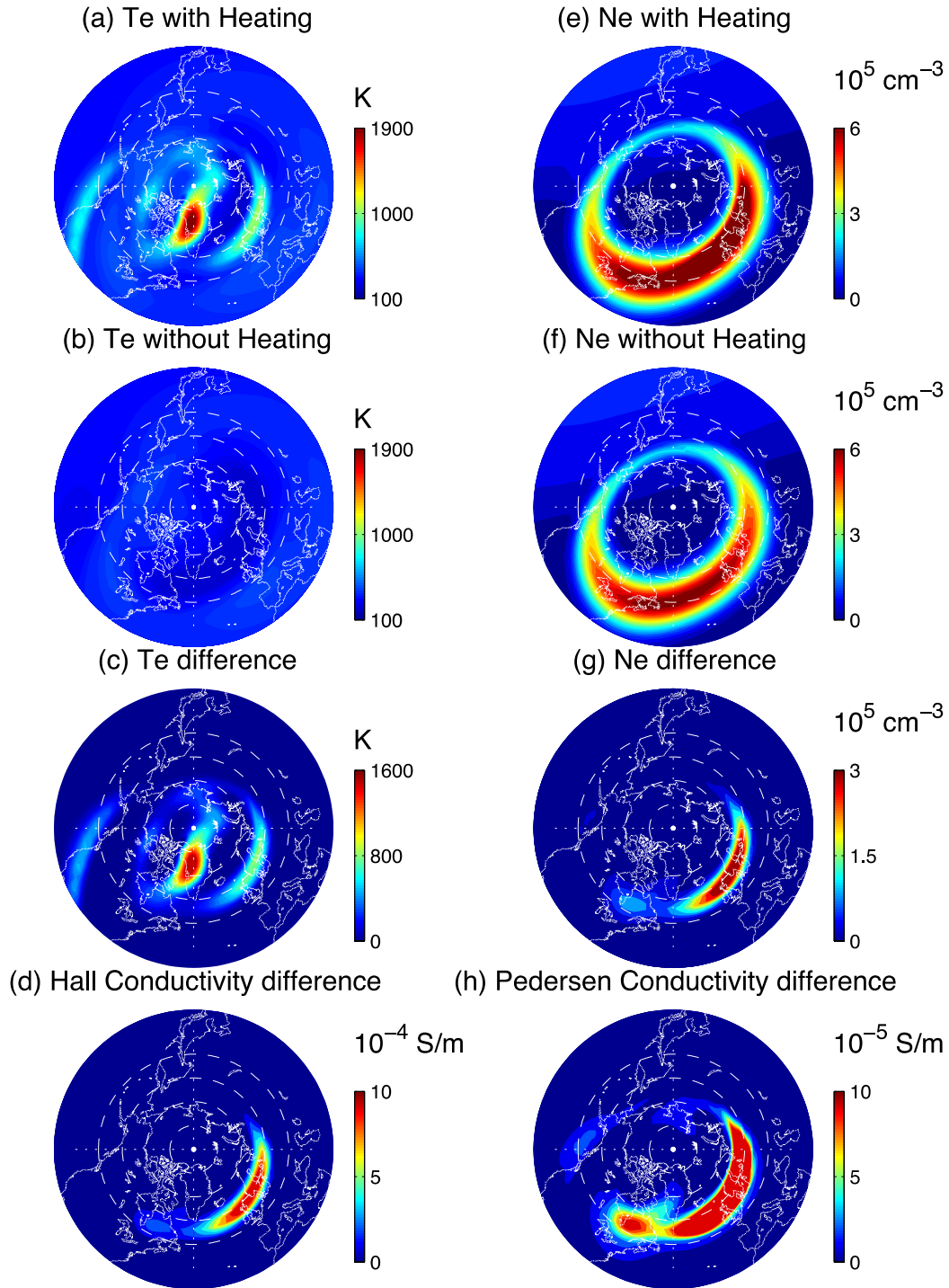
361
362
363

Figures



364
365
366
367
368
369
370

Figure 1. Polar views of (a) regular electron Ohmic energy deposition, (b) anomalous electron energy deposition, (c) TIEGCM auroral precipitation energy deposition in the Northern Hemisphere at 0300 UT in units of $\text{J}\cdot\text{m}^{-3}\cdot\text{s}^{-1}$, and (d) convection electric fields in units of mV/m at the -4.375 pressure level (~ 112 km). The perimeter latitude is 30° .



371
 372
 373
 374
 375
 376

Figure 2. Polar projections of (a-c) electron temperatures and (d-f) electron densities in geographic coordinates from TIEGCM simulations with or without AEH at 0300 UT at the - 4.375 pressure level (~112 km). Te and Ne differences of these two simulations are shown in Figures 2c and 2f, respectively. Hall and Pedersen Conductivity differences are shown in Figures 2d and 2f, respectively.

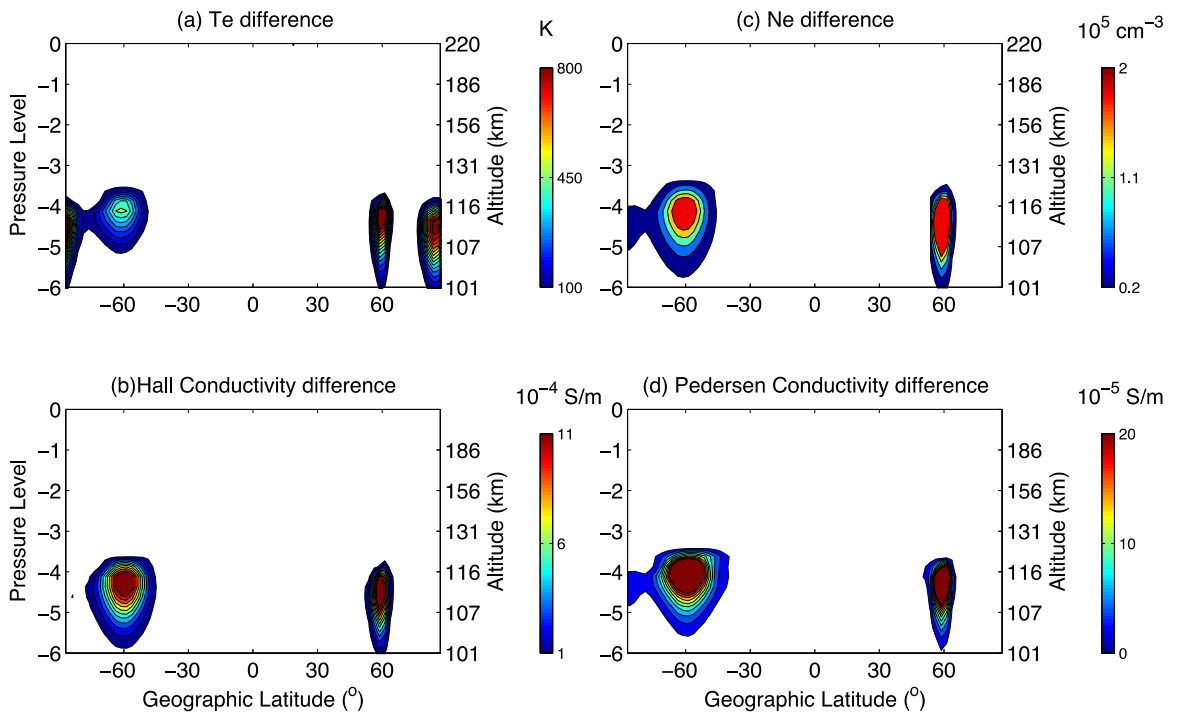
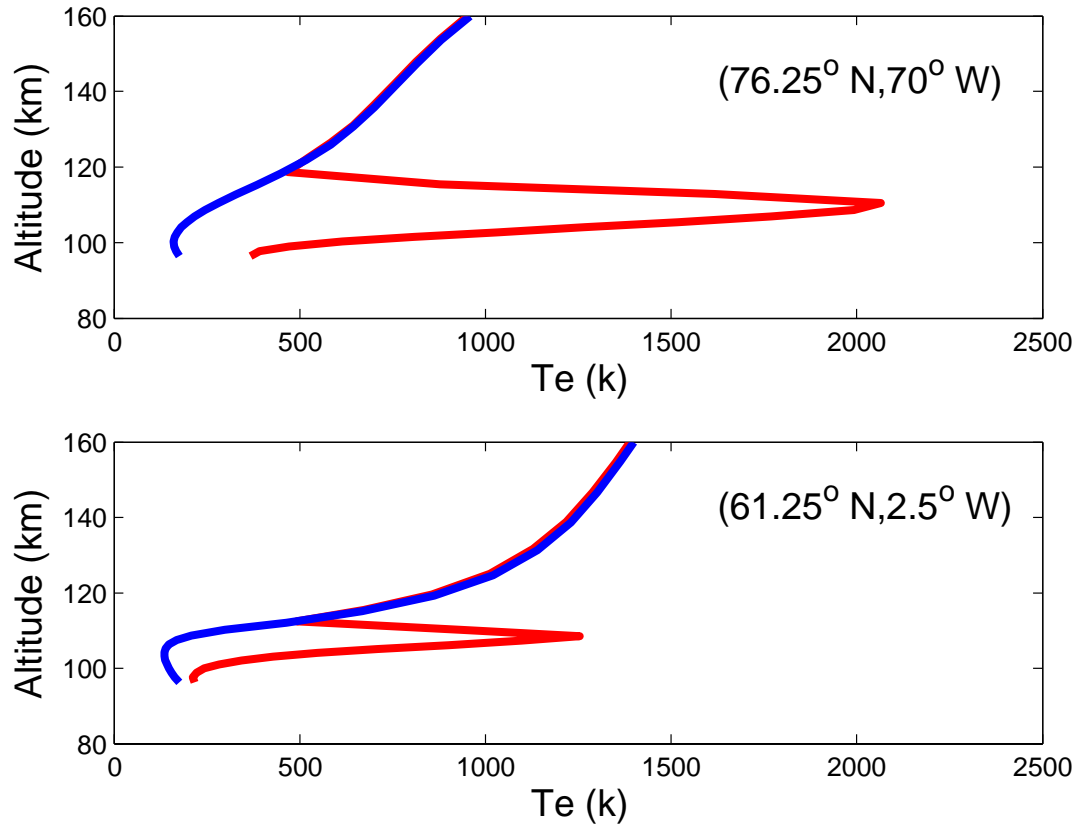


Figure 3. Latitudinal slices of differences in Te (Figure 3a, K), Ne (Figure 3c, cm^{-3}), Hall (Figure 3b, S/m) and Pedersen conductivity (Figure 3d, S/m) from TIEGCM simulations with and without AEH at 0400 LT.

377
 378
 379
 380
 381
 382
 383
 384
 385
 386
 387
 388
 389
 390
 391
 392
 393
 394
 395
 396
 397
 398
 399



400
 401 Figure 4. Electron temperature profiles at two locations (their coordinates are specified in the
 402 top right corner), corresponding to the two hot Te spots shown in Figure 2. The blue lines
 403 denote the results from the default TIEGCM run and the red lines are the results from the
 404 TIEGCM-k run.
 405
 406